

Parameters of two low-mass contact eclipsing binaries near the short-period limit

M. E. Lohr¹, S. T. Hodgkin², A. J. Norton¹, and U. C. Kolb¹

¹ Department of Physical Sciences, The Open University, Walton Hall, Milton Keynes MK7 6AA, UK
e-mail: Marcus.Lohr@open.ac.uk

² Institute of Astronomy, Madingley Road, Cambridge CB3 0HA, UK

Received 21 May 2013 / Accepted 31 January 2014

ABSTRACT

The two objects 1SWASP J150822.80–054236.9 and 1SWASP J160156.04+202821.6 were initially detected from their SuperWASP archived light curves as candidate eclipsing binaries with periods close to the short-period cut-off of the orbital period distribution of main sequence binaries, at ~ 0.2 d. Here, using INT spectroscopic data, we confirm them as double-lined spectroscopic and eclipsing binaries, in contact configuration. Following modelling of their visual light curves and radial velocity curves, we determine their component and system parameters to precisions between ~ 2 and 11%. The former system contains 1.07 and 0.55 M_{\odot} components, with radii of 0.90 and 0.68 R_{\odot} respectively; its primary exhibits pulsations with period 1/6 the orbital period of the system. The latter contains 0.86 and 0.57 M_{\odot} components, with radii of 0.75 and 0.63 R_{\odot} respectively.

Key words. stars: individual: 1SWASP J150822.80–054236.9 - stars: individual: 1SWASP J160156.04+202821.6 - binaries: close - binaries: eclipsing - binaries: spectroscopic

1. Introduction

The orbital period distribution of main sequence binary stars exhibits a fairly sharp lower limit at around 0.2 d (Rucinski 1992, 2007; Szymański et al. 2001; Paczyński et al. 2006), the cause of which is the subject of ongoing research e.g. Stepień (2006); Stepień & Gazeas (2012); Jiang et al. (2012). However, despite the inherent interest of this region of parameter space, relatively few eclipsing binaries (EB) have been discovered with periods near the cut-off point. This motivated a search of the archive of the SuperWASP project (Wide Angle Search for Planets: Pollacco et al. (2006)) for EB candidates with apparent periods $< 20\,000$ s (~ 0.2315 d), reported in Norton et al. (2011). 53 candidates were found, 48 of which were new discoveries at the time. A subsequent search of these candidate EBs for evidence of period change (Lohr et al. 2012) corrected the periods of nine to values slightly greater than 20 000 s, but still $< 22\,600$ s (~ 0.2616 d). A more rigorous search of the SuperWASP archive (Lohr et al. 2013) then detected 143 candidate EBs with periods $< 20\,000$ s, including 97 new discoveries since Norton et al. (2011), and measured significant period changes in 74 candidates.

Here, spectroscopic data allow us to confirm two of these candidates as double-lined EBs in contact configuration (WUMa-type variables): 1SWASP J150822.80–054236.9 (J150822) and 1SWASP J160156.04+202821.6 (J160156). Both were initially identified in Norton et al. (2011); the period of J150822 was revised upwards to 22469.2 s in Lohr et al. (2012) and so it did not appear in Lohr et al. (2013). We report system and component parameters obtained for these EBs by simultaneous modelling of their SuperWASP light curves and radial velocities. These should be of interest for the study of low-mass dwarfs and WUMa systems in general, and of very short period binaries specifically.

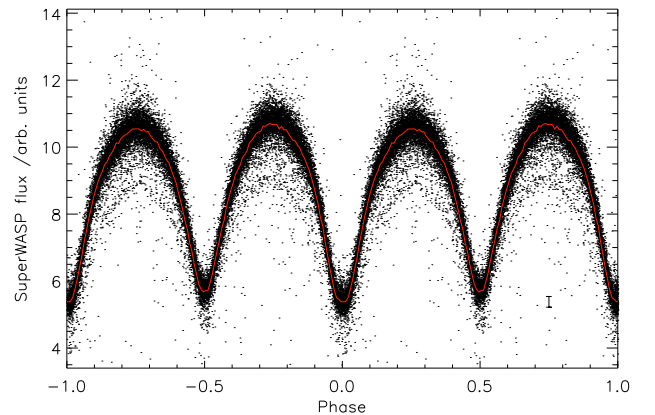


Fig. 1. SuperWASP light curve for J150822, folded at period of 22469.219 s, with binned mean curve overlaid. A typical uncertainty range for a single observation is shown. These fluxes correspond to a visual magnitude range of ~ 12.4 – 13.2 .

2. Observations

2.1. Photometry

The SuperWASP archive contains 30131 photometric points for J150822, taken between 5 March 2008 and 29 March 2011. For J160156 there are 14651 observations, made between 2 May 2004 and 21 February 2011. Sys-Rem-corrected fluxes (Tamuz et al. 2005; Mazeh et al. 2006) from the 3.5 pixel-radius photometric aperture (the middle of three available apertures) were used to construct the light curves used here, which correspond approximately to the Johnson V band. Periods and period-change measurements were obtained using a custom-

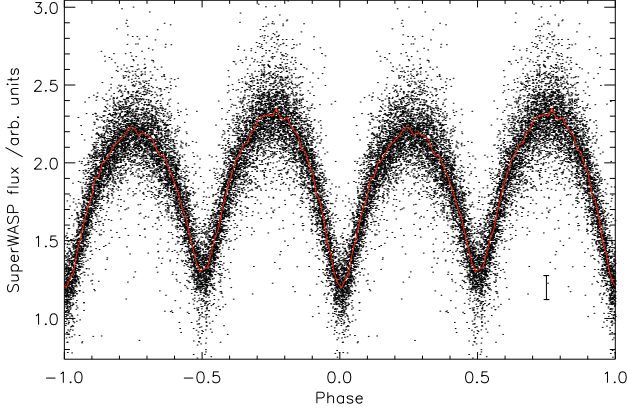


Fig. 2. SuperWASP light curve for J160156, folded at period of 19572.136 s, with binned mean curve overplotted. A typical uncertainty range for a single observation is shown. These fluxes correspond to a visual magnitude range of ~ 14.1 – 14.8 .

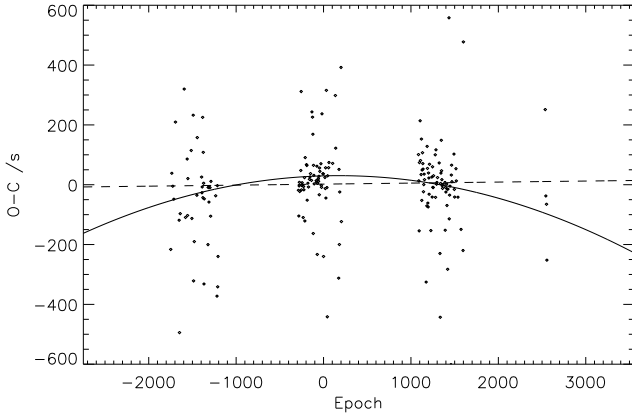


Fig. 3. Observed minus calculated (O–C) diagram for J150822, with best linear (dashed line; $\chi^2 = 5.25$) and quadratic (solid curve; $\chi^2 = 4.87$) fits overplotted. For clarity of presentation, uncertainties are not shown. Period decrease of $-0.055 \pm 0.006 \text{ s y}^{-1}$ is indicated ($\sigma = 8$).

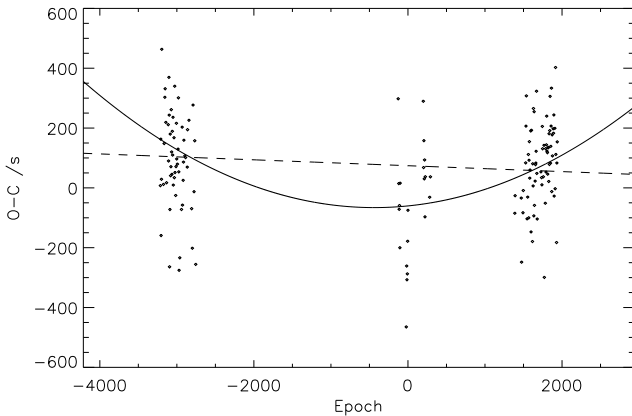


Fig. 4. O–C diagram for J160156, with best linear (dashed line; $\chi^2 = 1.87$) and quadratic (solid curve; $\chi^2 = 1.64$) fits overplotted. For clarity of presentation, uncertainties are not shown. Period increase of $+0.094 \pm 0.015 \text{ s y}^{-1}$ is indicated ($\sigma = 6$).

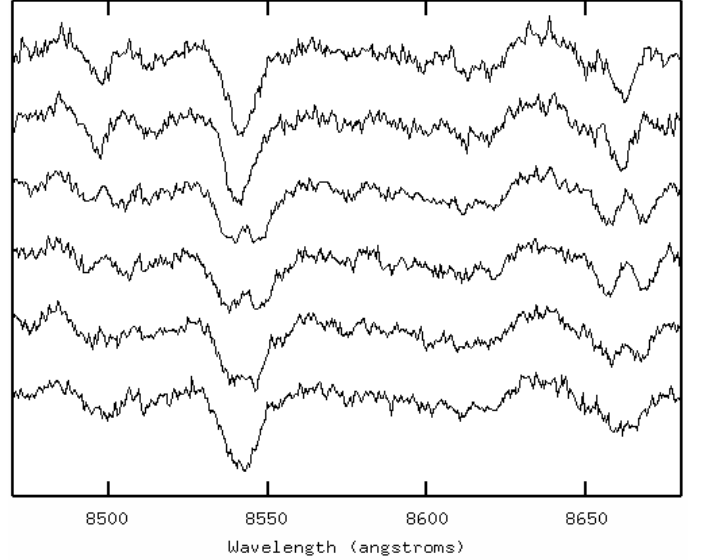


Fig. 5. Selected spectra in region of Ca II triplet (laboratory wavelengths: 8498.03, 8542.09 and 8662.14 Å) for J150822, taken from final night of observations. Line splitting is readily apparent for all three calcium lines.

written IDL program, as described in Lohr et al. (2013), and the binned averaged phase-folded data produced high-precision phased light curves (Figs. 1 to 4). A small secular period decrease (-0.055 s y^{-1}) was measured for J150822, and a slightly larger secular period increase (0.094 s y^{-1}) for J160156; both values are fairly unexceptional for variables of this type (Lohr et al. 2013). The scatter here is comparable to that seen in other SuperWASP light curves for objects of similar magnitude, and we do not believe that either period variation over time, or flux variability caused by surface spots, contribute to it significantly. The uncertainties on the means in the light curves used in subsequent modelling were given by the standard deviation of points in each bin, divided by the square root of the number of observations per bin i.e. σ / \sqrt{n} .

2.2. Spectroscopy

36 long-slit spectra were obtained for J150822, and 28 for J160156, with the Intermediate Dispersion Spectrograph (IDS) on the 2.5 m Isaac Newton Telescope at La Palma in the Canary Islands. The observations for the two stars were interspersed with each other, and covered three consecutive nights (11–13 March 2012), to optimise phase coverage. Exposures were 300 or 600 s to allow for the short orbital periods involved, and a wavelength range of ~ 7915 – 9040 Å was chosen, which covers the Ca II triplet. The RED+2 CCD and R1200R gratings were used, providing a resolution of 0.51 Å per pixel. S/N values of ~ 40 – 50 were obtained around quadrature for J150822, and ~ 30 – 40 for J160156. The spectra were flat-fielded, bias-corrected and optimally extracted using standard IRAF routines, and calibrated using CuArNe arc lamp exposures.

Line splitting was clearly observable by eye (Figs. 5 and 6) and could be used to estimate phase. A suitable synthetic comparison spectrum was then selected by cross-correlation with a phase 0 program spectrum; the best-matching template for both objects had a temperature of 4500 K. Radial velocities were measured by cross-correlation with the template, using the IRAF task

Table 1. Summary of spectroscopic observations and derived quantities for J150822

HJD -2450000	Phase	Primary RV (km s ⁻¹)	δ Primary RV (km s ⁻¹)	Secondary RV (km s ⁻¹)	δ Secondary RV (km s ⁻¹)	Continuum flux at 8500 Å (arb. units)
5997.5934	0.302	^a				2995
5997.5977	0.319	-128	24	242	37	2858
5997.6015	0.333	-117	26	248	34	2342
5997.6406	0.484					1115
5997.6444	0.498					1202
5997.6482	0.513					1346
5997.6756	0.618	46	29	-203	36	3682
5997.6792	0.632	70	38	-191	45	3852
5997.6829	0.646	109	30	-233	27	3678
5997.7080	0.743	118	33	-265	23	4034
5997.7119	0.758	126	31	-265	23	3978
5997.7155	0.772	118	36	-257	24	4278
5998.6826	0.490					2050
5998.6863	0.504					2095
5998.7272	0.661	127	28	-221	30	2196
5998.7309	0.676	100	37	-237	25	3401
5998.7348	0.691	126	28	-239	23	3530
5998.7571	0.776	145	24	-243	28	4294
5998.7613	0.793	130	29	-245	24	4143
5998.7650	0.807	139	23	-227	31	3403
5999.5733	0.915	69	22	-117	22	2737
5999.5770	0.929					2689
5999.5806	0.943					2459
5999.6170	0.083	-85	18	86	21	2965
5999.6244	0.111	-86	23	131	26	3316
5999.6316	0.139	-111	30	190	30	3613
5999.6680	0.279	-143	24	253	27	4167
5999.6765	0.312	-147	27	237	27	3810
5999.6850	0.344	-131	29	235	31	3744
5999.7209	0.482					1954
5999.7282	0.510	0	13			1754
5999.7356	0.539					2014
5999.7681	0.664	116	26	-219	27	3669
5999.7719	0.678	121	29	-224	30	3737
5999.7755	0.692	121	27	-269	21	3582
5999.7804	0.711	138	21	-248	25	3802

Notes. ^(a) Radial velocities unusable.

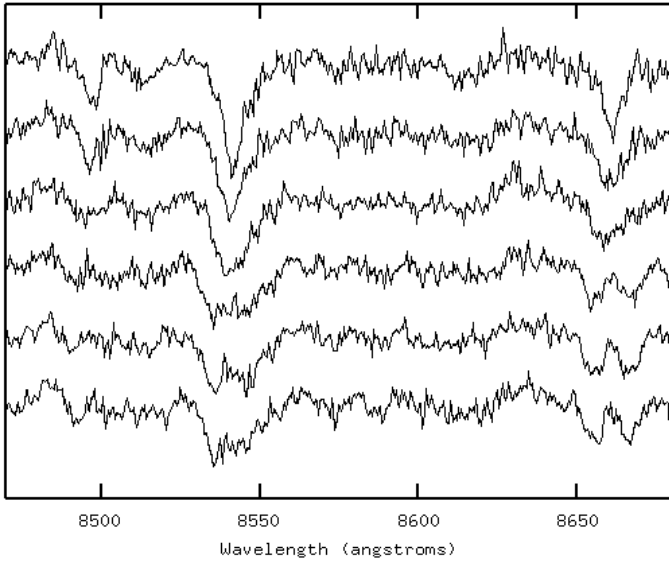


Fig. 6. Selected spectra in region of Ca II triplet for J160156, taken from final night of observations. Line splitting is most obvious for the two calcium lines at longer wavelengths.

FXCOR. Uncertainties were minimized by excluding the broadest Ca II line from consideration. Improved phase determinations were obtained by fitting sinusoidal functions to the RV curves to locate cross-over points corresponding to phases 0 and 0.5.

These phasings were then compared with the predictions of the SuperWASP linear and quadratic ephemerides (implying constant periods and secular period change respectively), and with internal simultaneous low-resolution light curves extracted from the spectra themselves (by evaluating a continuum fit at 8500 Å), and were found to be substantially self-consistent (Figs. 7 and 8). The divergence between different phase measures is greater for J160156; this is a consequence of its shorter period, more rapid predicted period change, smaller data sets (both photometric and spectroscopic) and longer time gap between the last archived photometry and the spectroscopy. It is notable that in each system the deeper minimum of the light curve corresponds to the eclipse of the secondary, less massive binary component; the SuperWASP light curves were consequently refolded to locate phase 0 at the time of true primary eclipse. The resulting spectroscopic observations and derived quantities are given in Tables 1 and 2. The velocity uncertainties are those obtained with FXCOR; uncertainties in phase (using

Table 2. Summary of spectroscopic observations and derived quantities for J160156

HJD -2450000	Phase	Primary RV (km s ⁻¹)	δ Primary RV (km s ⁻¹)	Secondary RV (km s ⁻¹)	δ Secondary RV (km s ⁻¹)	Continuum flux at 8500 Å (arb. units)
5997.6567	0.923					635
5997.6605	0.940					765
5997.6643	0.957					702
5997.6902	0.071					858
5997.6939	0.087					925
5997.6976	0.104	-68	26	133	27	909
5998.7083	0.565					594
5998.7120	0.582	58	20	-133	20	637
5998.7157	0.598	97	20	-96	21	628
5998.7401	0.706	180	23	-223	31	1087
5998.7439	0.722	169	18	-226	22	1107
5998.7499	0.749	168	28	-218	19	1102
5998.7718	0.846	128	22	-190	23	1062
5998.7768	0.868	135	29	-193	22	1062
5998.7806	0.884	156	27	-126	31	983
5998.7851	0.904	144	17	-30	41	933
5999.5888	0.452	7	18			410
5999.5968	0.487					593
5999.6039	0.519					584
5999.6409	0.682	151	25	-203	20	1080
5999.6481	0.714	141	23	-218	19	1110
5999.6553	0.746	167	27	-219	20	1143
5999.6945	0.919					879
5999.7033	0.958					761
5999.7105	0.989	-8	9			680
5999.7439	0.137	-125	26	165	27	903
5999.7512	0.169	-142	21	219	23	937
5999.7583	0.200	-150	25	229	26	957

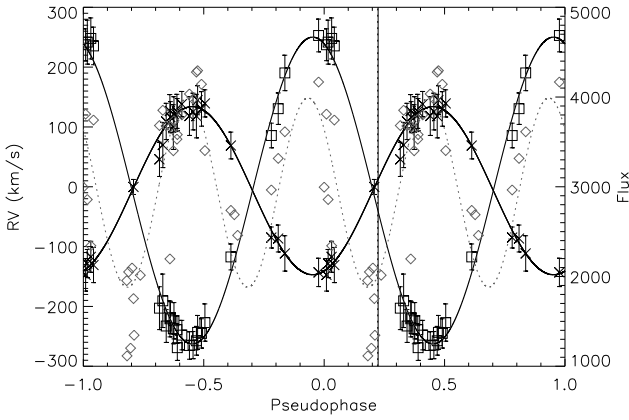


Fig. 7. Radial velocities for J150822 (crosses indicate primary component, squares secondary) with preliminary fits (solid curves) used to obtain correct phasing of observations. Also shown are a light curve obtained from the spectra themselves (grey diamonds, fitted with dotted grey curve) and the predictions for time of minimum light from SuperWASP ephemerides (solid vertical line indicates linear ephemeris i.e. no period change, dotted vertical line quadratic i.e. secular period change; the two are almost coincident).

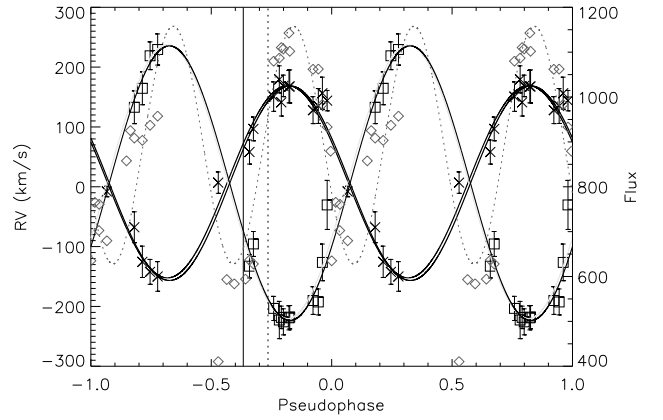


Fig. 8. Radial velocities for J160156 (crosses indicate primary component, squares secondary) with preliminary fits (solid curves) used to obtain correct phasing of observations. The primary and secondary curve fits were determined consecutively, with the second fit deriving some parameters from the first, and then refitted in the other order; this has resulted in the visibly double fit curve for the primary component. Also shown are a light curve obtained from the spectra themselves (grey diamonds, fitted with dotted grey curve) and the predictions for time of minimum light from SuperWASP ephemerides (solid vertical line indicates linear ephemeris, dotted vertical line quadratic).

3. Results

the sinusoidal fitting described above) are negligible in comparison, and were not included in subsequent modelling.

The eclipsing binary modelling software PHOEBE (Prša & Zwitter 2005), built upon the code of

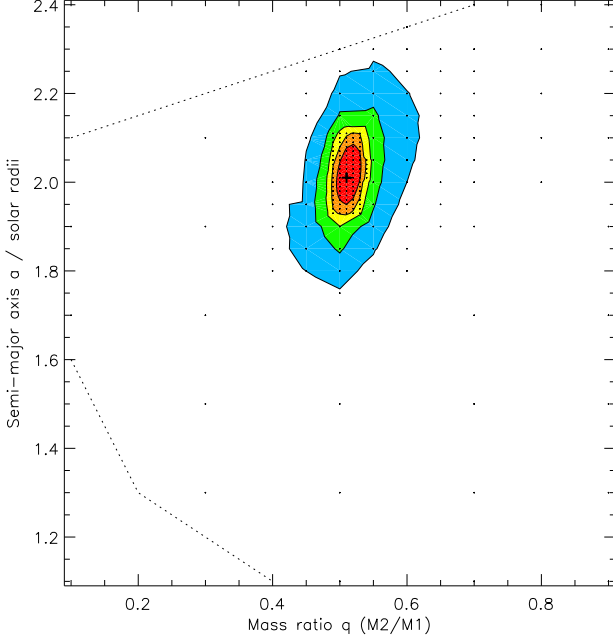


Fig. 9. a - q parameter cross-section for J150822. Boxes indicate points sampled (other parameters being optimized) and the global minimum is marked with a cross. Contour lines show the 1, 2, 3, 4 and 5 σ uncertainty levels, derived from the $\Delta\chi^2$ values of the sampled points. Points outside the plot boundaries or the dotted lines were not sampled since they corresponded to physically-implausible masses for the stellar components (<0.08 or $>1.5 M_{\odot}$).

Wilson & Devinney (1971), was used to model simultaneously the binned SuperWASP light curves and INT radial velocity curves of the two systems. (The full SuperWASP light curves were also modelled as a final check on the validity of the optima found using binned curves; it would have been prohibitively time-consuming to carry out the full modelling procedure using curves consisting of tens of thousands of data points.) A semi-detached or contact configuration (one or both components overflowing their Roche lobes) was assumed on the basis of the continuous light variation in the light curves, so the Unconstrained mode was used to allow for both possibilities. An approximate shared temperature (which would correspond to the envelope surrounding the components of a W UMa-type system) of 4500 ± 250 K was used for both EBs, because a template with this effective temperature had provided the best match for phase 0 and phase 0.5 spectra during radial velocity determination; this was not varied during modelling due to the relatively low S/N of the spectroscopic data and the limited contribution of temperature to the goodness of model fit.

The shortness of the orbital periods involved constrained us to sub-solar or approximately solar parameters for masses and radii: large stars simply would not fit into the orbits implied, and so trial values of semi-major axis were limited accordingly. No third light was included since in each light curve the deeper eclipse has roughly half the flux of the higher maximum. The details of light curve shape also constrained the possible angles of inclination: J150822 has slightly flattened eclipse bottoms, implying i close to 90° , while J160156 has more pointed eclipse bottoms, ruling out such a high angle. The shapes of the ‘shoulders’ of the maxima in each case implied Kopal potentials lower

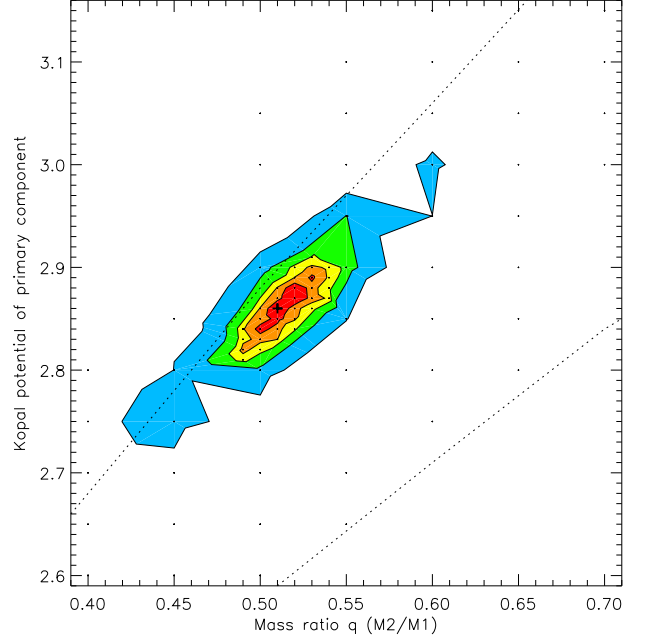


Fig. 10. Ω_1 - q parameter cross-section for J150822. Points below the lower dotted line were not sampled since they corresponded to physically-implausible filling factors ($F > 1$); very high potentials, corresponding to highly unlikely detached configurations, were also not sampled. The upper dotted line indicates the location of the binary’s Roche lobe; the primary component is (with high probability) just below this line, and hence is likely to be just overflowing the Roche lobe.

than the critical potential at Lagrange point L_1 i.e. yielding binary filling factors in (0,1], using Prša’s definition

$$F = \frac{\Omega - \Omega_{\text{crit}}^{L_1}}{\Omega_{\text{crit}}^{L_2} - \Omega_{\text{crit}}^{L_1}}. \quad (1)$$

The radial velocity curve amplitudes alone determined the semi-major axes of the orbits a and hence the absolute sizes of the components, while their mass ratios q were constrained by both light and radial velocity curves, via the relative eclipse depths and relative amplitudes of primary and secondary components. The light curves provided most of the information needed to determine the optimum angles of inclination i and Kopal potentials $\Omega_{1,2}$.

Using these guidelines, and following a similar approach to that of Chew (2010), an initial best-fit solution was found manually for each system, which minimized the combined χ^2 values for the light curve and the two radial velocity curves. To ensure that these solutions corresponded to global rather than local minima, to explore the correlations between fitting parameters, and to determine realistic uncertainties for the best-fit parameter values, a series of heuristic scans of the five-dimensional parameter space (a , q , i and $\Omega_{1,2}$) were carried out using the PHOEBE scripter. Initially the entire physically-plausible parameter space was scanned with widely-spaced grids, to ensure that no regions of low χ^2 values had been missed. The scans were then repeated with decreasing grid spacings, focusing on regions where the difference $\Delta\chi^2 = \chi^2 - \chi_{\text{min}}^2$ corresponded to an uncertainty below 3σ (Press et al. 2007), until the position of the minimum was determined with accuracy.

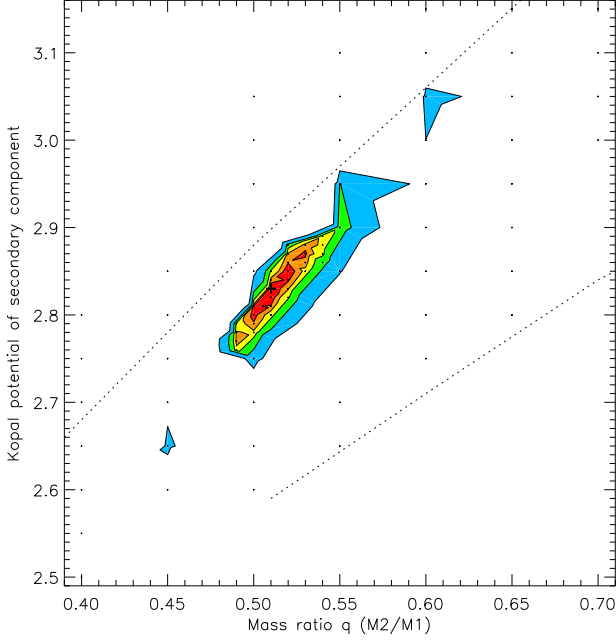


Fig. 11. Ω_2 - q parameter cross-section for J150822 (see caption to Fig. 10 for explanation of dotted lines). The secondary component is, with very high probability, overfilling the Roche lobe.

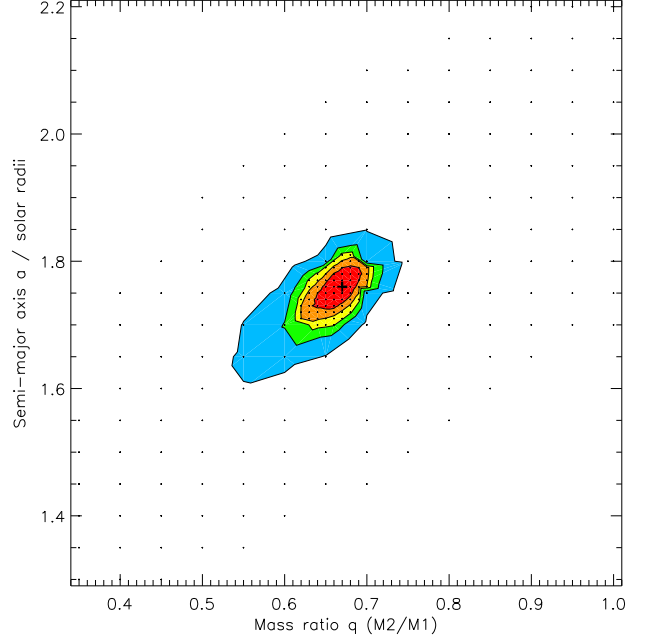


Fig. 13. a - q parameter cross-section for J160156. A fairly strong correlation between semi-major axis and mass ratio is apparent.

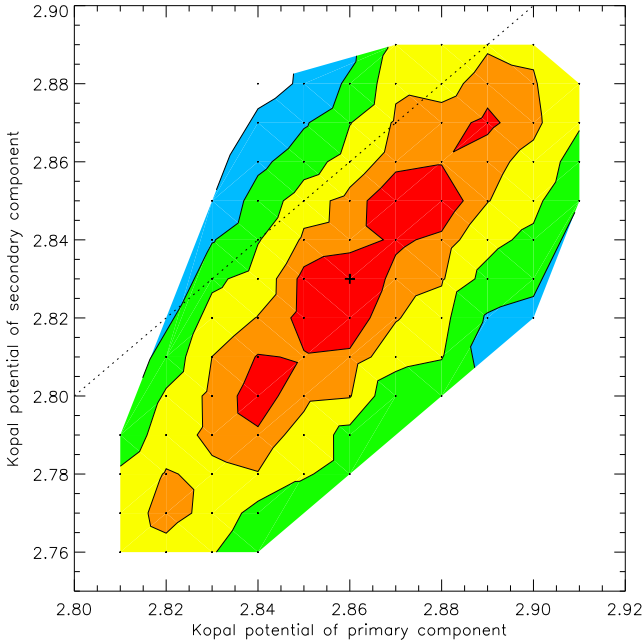


Fig. 12. Ω_1 - Ω_2 parameter cross-section for J150822. The dotted line here indicates equal potentials for the two components, which would necessarily be the case in a contact system; their probability distribution nearly follows this line, showing a strong correlation between Ω_1 and Ω_2 .

The global optima found for the two systems via the scans were very close to those found manually; the combined minimum χ^2 value for J150822 was 2.36 and for J160156 was 4.72. Since these values were far greater than 1, indicating poor model fits (for reasons explored below), the $\Delta\chi^2$ value at which to set

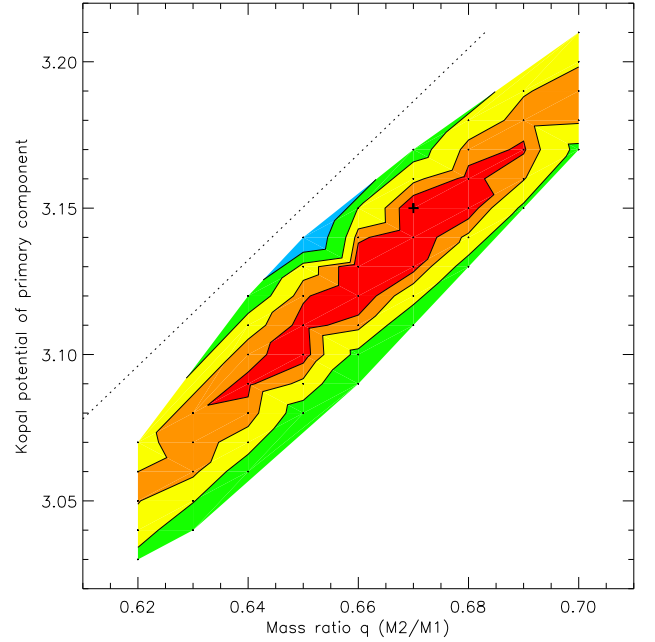


Fig. 14. Ω_1 - q parameter cross-section for J160156. The dotted line indicates the location of the binary's Roche lobe; the primary component is with high probability below this line, and hence is very likely to be overfilling the Roche lobe.

the 1σ uncertainty boundary was set with the assistance of a separate series of manually-determined optimal solutions for simulated data sets, with data points randomly perturbed according to their original individual uncertainties. The standard deviations of the parameters, estimated by this method, were comparable in size to the formal uncertainties given by the Wilson-Devinney covariance matrix.

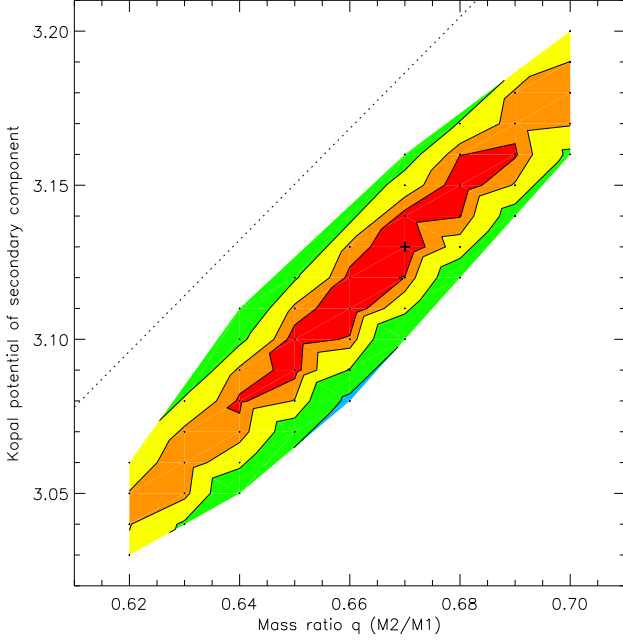


Fig. 15. Ω_2 - q parameter cross-section for J160156. The secondary component is also very likely to be overfilling the Roche lobe.

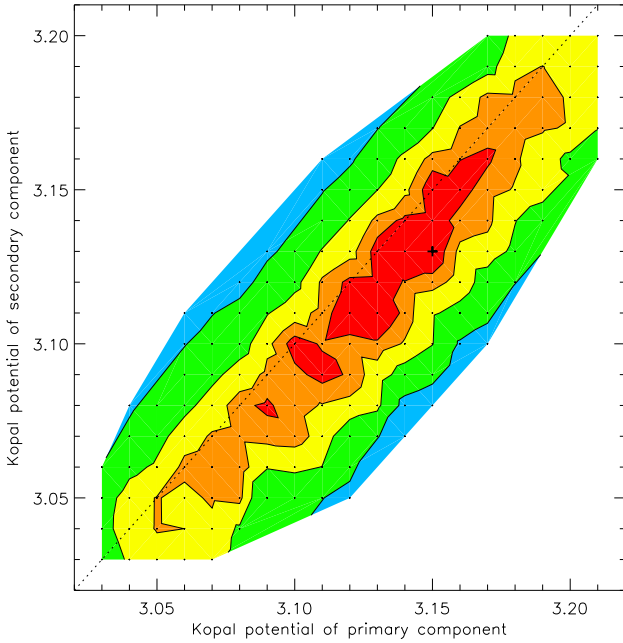


Fig. 16. Ω_1 - Ω_2 parameter cross-section for J160156. The region of highest probability closely follows the dotted line, suggesting near-identical potentials for the two components.

Figs. 9–16 illustrate some of the 10 two-dimensional parameter cross-sections obtained from the scans. The $\Omega_{1,2}$ - q planes are particularly revealing: both systems have best-fit solutions in which both components overfill their Roche lobes, and where the two potentials are strongly correlated with each other (Figs. 12 and 16), suggesting the components of each system share a common potential within the shared envelope of a contact binary.

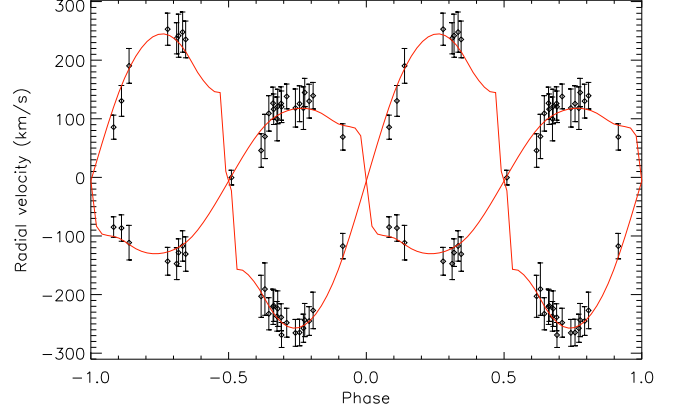


Fig. 17. Radial velocity curves for J150822 with best-fit model overplotted.

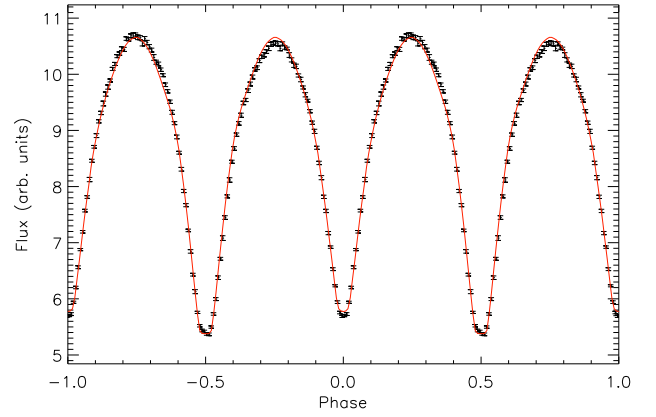


Fig. 18. SuperWASP binned light curve for J150822 with best-fit unspotted model overplotted.

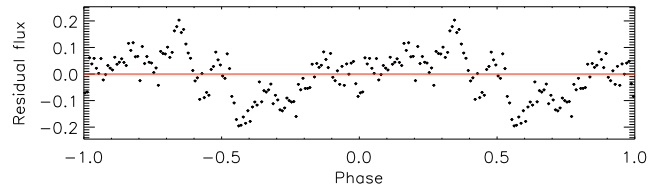


Fig. 19. Light curve residuals for J150822 best-fit model.

Figs. 17 to 28 show the best-fit PHOEBE models for the two systems. A small Rossiter-McLaughlin effect (Rossiter 1924; McLaughlin 1924) is seen in the model for J150822 in the asymmetry of the radial velocity curves (Fig. 17); this is a consequence of the high angle of inclination. The different heights of maxima visible in both light curves, but most notably in J160156, are most likely attributable to star spots i.e. the O’Connell effect (O’Connell 1951). However, since we lack any direct evidence for the number, size or location of spots (e.g. via Doppler tomography), and being mindful of the additional modelling latitude provided by inclusion of spots, we sought to determine the best-fit model for the light curves without including any spots, and our final stellar parameters result from this model. Figs. 20 and 26 indicate the improvement of fit resulting

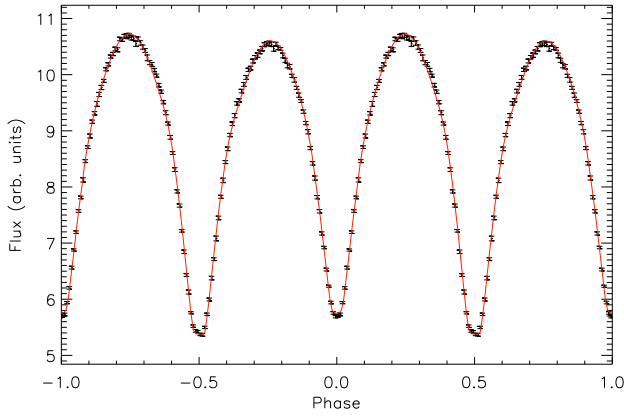


Fig. 20. Best-fit model for J150822 with example spot included.

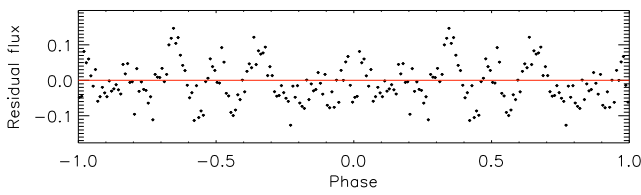


Fig. 21. Light curve residuals for J150822 example model with single cool spot.

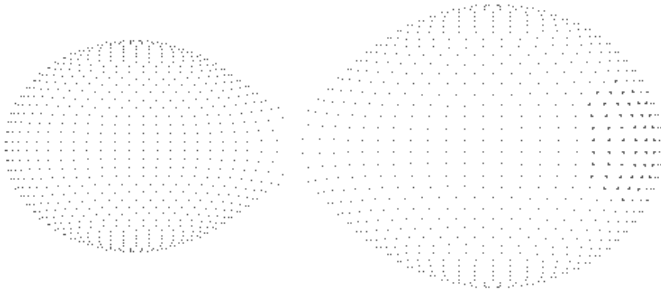


Fig. 22. Image of J150822 PHOEBE best-fit model at phase 0.75, indicating location and size of example cool spot on primary.

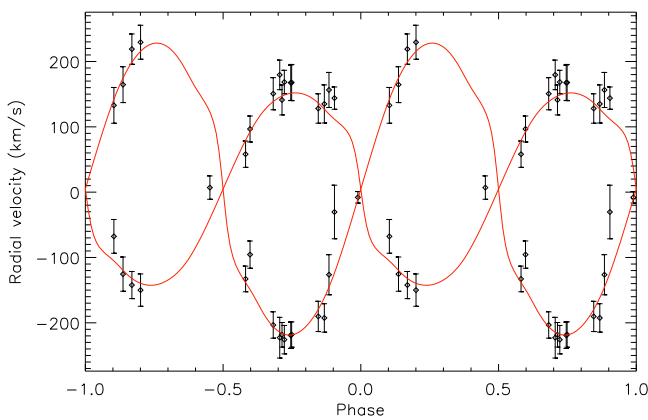


Fig. 23. Radial velocity curves for J160156 with best-fit model overplotted.

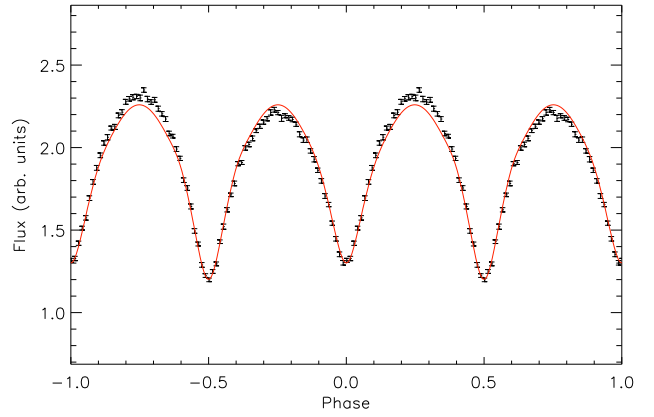


Fig. 24. SuperWASP binned light curve for J160156 with best-fit unspotted model overplotted.

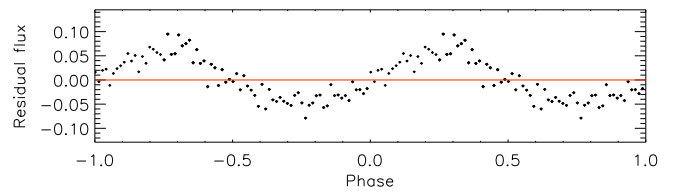


Fig. 25. Light curve residuals for J160156 best-fit model.

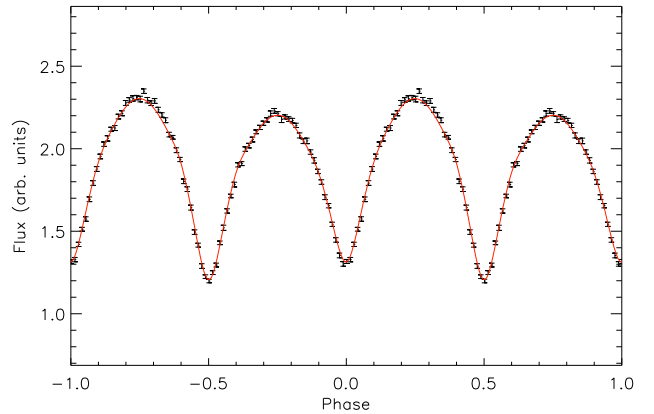


Fig. 26. Best-fit model for J160156 with example spot included.

from adding a single cool spot to the primary component in each system, without altering any other input parameters. Figs. 22 and 28 show the appearance of the modelled spotted systems, which reproduce both the different heights of maxima and the different depths of minima better than the unspotted models can. Addition of further spots could doubtless produce a perfect match of models to light curves, but at the expense of the plausibility of the modelling.

The residuals for the light curve fits reflect these assumed spots in their large-scale sinusoidal deviations (Figs. 19 and 25). However, there are additional clear sinusoidal variations at a smaller scale in the residuals for J150822 (Fig. 21): an oscillation with an amplitude of around ± 0.1 flux units and a frequency of six cycles per orbit. Presumably these correspond to pulsation of the primary (since they are obscured during primary eclipse),

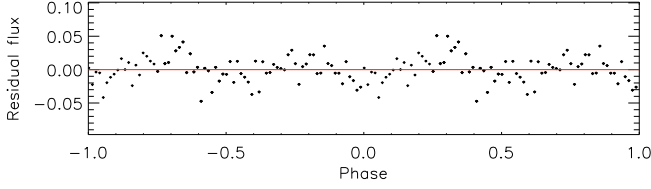


Fig. 27. Light curve residuals for J160156 example model with single cool spot.

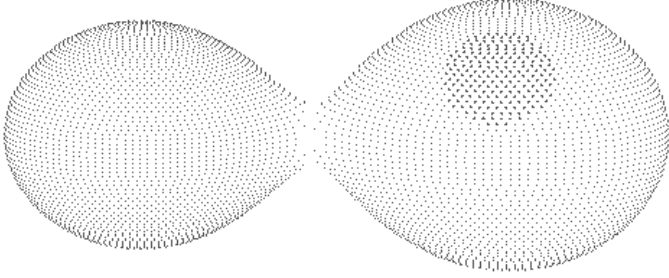


Fig. 28. Image of J160156 PHOEBE best-fit model at phase 0.75, indicating location and size of example cool spot on primary.

Table 3. Modelled system and stellar component parameters for J150822 and J160156

		J150822	J160156
Semi-major axis (R_{\odot})	a	$2.01^{+0.07}_{-0.06}$	1.76 ± 0.03
Mass ratio	M_2/M_1	$0.51^{+0.02}_{-0.01}$	$0.67^{+0.02}_{-0.03}$
COM velocity (km s^{-1})	V_0	$-6.2^{+2.8}_{-2.5}$	$4.7^{+1.8}_{-1.2}$
Angle of incl. ($^{\circ}$)	i	90^{+0}_{-3}	79.5 ± 0.25
Kopal potentials	Ω_1	$2.86^{+0.03}_{-0.02}$	$3.15^{+0.02}_{-0.06}$
	Ω_2	2.83 ± 0.04	$3.13^{+0.03}_{-0.05}$
Filling factor	\mathcal{F}	$0.12^{+0.06}_{-0.04}$	$0.10^{+0.06}_{-0.00}$
Masses (M_{\odot})	M_1	$1.07^{+0.12}_{-0.09}$	0.86 ± 0.04
	M_2	$0.55^{+0.06}_{-0.05}$	0.57 ± 0.04
Radii (R_{\odot})	R_1	$0.90^{+0.05}_{-0.03}$	0.75 ± 0.01
	R_2	0.68 ± 0.03	0.63 ± 0.02

and are locked to the binary orbital period (since they are clearly visible in the folded light curve).

The final best-fit parameters for both systems are given in Table 3. We would emphasise that these parameters are not dependent on the inclusion of spots in the models. The uncertainties on a , q , i and $\Omega_{1,2}$ were obtained from the 1σ contours in the relevant parameter cross-sections. The uncertainties on the output parameters (masses and radii) are the maximum/minimum values obtainable using parameter combinations falling within these 1σ contours.

4. Discussion

These results confirm J150822 and J160156, initially identified as candidate EBs on the basis of light curve shapes alone, as double-lined spectroscopic and eclipsing binaries. From modelling, both systems appear to be composed of late G–early M class dwarfs. J150822 is slightly more massive, with an approximately solar-mass primary and late K secondary; its masses have been determined with a precision of $\sim 10\%$ and its radii within $\sim 4\%$. J160156’s components are of more similar mass: a late G or early K primary and a late K or early M secondary; its

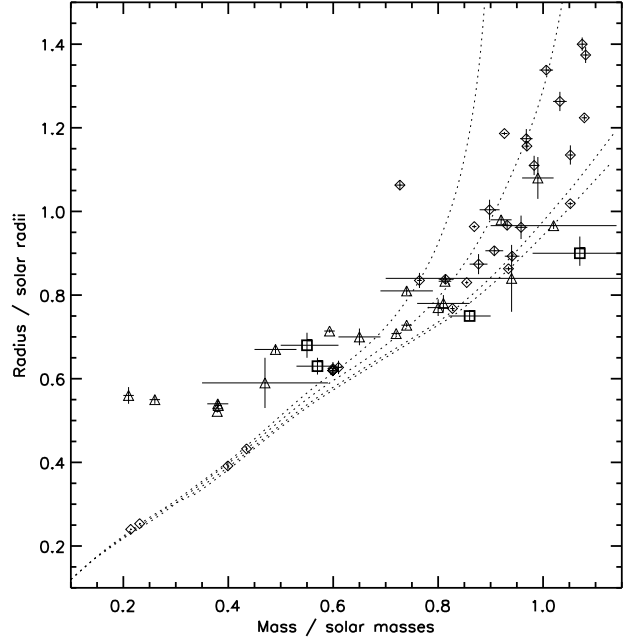


Fig. 29. Masses vs. radii of J150822 and J160156 components (squares) compared with 32 components of low-mass detached binaries (diamonds) from Torres et al. (2010), and 20 components of short-period contact binaries (triangles) from Stepień & Gazeas (2012). Also plotted are theoretical isochrones derived from Dartmouth models (Dotter et al. 2008), for solar metallicity, with ages of 0.25, 1, 5 and 10 Gyr respectively (dotted lines, ascending).

masses have been found with a precision of $\sim 5\%$ and its radii within $\sim 2\%$. Both appear to be W-type systems, in the sense of Binnendijk (1970), in that the less massive component is eclipsed during the deeper minimum.

The contact configuration and likely mass exchange associated with the apparent period changes make it difficult to compare directly the mass-radius relationships of these systems with those collected and discussed in e.g. Torres et al. (2010) (Fig. 2) and Torres (2013) (Fig. 4) for detached binaries containing low-mass components. Fig. 29 therefore compares our results both with those of Torres et al. and of a selection of short-period contact systems collected by Stepień & Gazeas (2012). We may note that, like several other contact systems, the binaries studied here are somewhat discrepant with the Dartmouth model isochrones for solar metallicity (Dotter et al. 2008)¹ models/. Specifically, the primaries have smaller radii than their masses might suggest, while the secondaries have larger radii than expected. Possibly the primaries’ less dense outer layers have been partially stripped and transferred to the secondaries, leaving denser “cores”. Higher resolution spectroscopy and/or Doppler tomography would be required for confirmation.

5. Conclusions

J150822 and J160156 are established to be spectroscopic double-lined and eclipsing binary systems in contact configuration, composed of low-mass dwarfs. J150822 has been modelled as consisting of 1.07 and 0.55 M_{\odot} components (mass ratio 0.51),

¹ <http://stellar.dartmouth.edu/~>

and J160156 as having 0.86 and 0.57 M_{\odot} components (mass ratio 0.67). The primary of J150822 appears to be pulsating with a period 1/6 of the orbital period. Both systems are plausibly undergoing mass transfer; this may be related to the primaries' radii being smaller, and the secondaries' radii being larger, than would be typical for single stars with these masses.

The parameters obtained here should contribute to our understanding of low-mass stars and contact binary systems, since relatively few binaries are known with such short orbital periods. We hope to follow up further candidate short-period EBs listed in Lohr et al. (2013) with multi-colour photometry and spectroscopy, with a view to confirming their binary nature. Many of them should be good prospects for full solution, and capable of significantly extending our knowledge of this aspect of the field.

Acknowledgements. The WASP project is funded and operated by Queen's University Belfast, the Universities of Keele, St. Andrews and Leicester, the Open University, the Isaac Newton Group, the Instituto de Astrofísica de Canarias, the South African Astronomical Observatory and by STFC. The Isaac Newton Telescope is operated on the island of La Palma by the Isaac Newton Group in the Spanish Observatorio del Roque de los Muchachos of the Instituto de Astrofísica de Canarias. This work was supported by the Science and Technology Funding Council and the Open University. We would like to thank the referee for constructive comments and recommendations which have improved this paper.

References

- Binnendijk, L. 1970, *Vistas in Astronomy*, 12, 217
- Chew, Y. G. M. 2010, On the analysis of two low-mass, eclipsing binary systems in the young Orion Nebula cluster (unpublished PhD thesis: Vanderbilt University)
- Dotter, A., Chaboyer, B., Jevremović, D., et al. 2008, *ApJS*, 178, 89
- Jiang, D., Han, Z., Ge, H., Yang, L., & Li, L. 2012, *MNRAS*, 421, 2769
- Lohr, M. E., Norton, A. J., Kolb, U. C., et al. 2012, *A&A*, 542, A124
- Lohr, M. E., Norton, A. J., Kolb, U. C., et al. 2013, *A&A*, 549, A86
- Mazeh, T., Tamuz, O., Zucker, S., et al. 2006, in Tenth Anniversary of 51 Peg-b: Status of and prospects for hot Jupiter studies. Colloquium held at Observatoire de Haute Provence, France, August 22-25, 2005, ed. L. Arnold, F. Bouchy, & C. Moutou (Paris: Frontier Group), 165–172
- McLaughlin, D. B. 1924, *ApJ*, 60, 22
- Norton, A. J., Payne, S. G., Evans, T., et al. 2011, *A&A*, 528, A90
- O'Connell, D. J. K. 1951, *Publications of the Riverview College Observatory*, 2, 85
- Paczyński, B., Szczygieł, D. M., Pilecki, B., & Pojmański, G. 2006, *MNRAS*, 368, 1311
- Pollacco, D. L., Skillen, I., Cameron, A. C., et al. 2006, *PASP*, 118, 1407
- Press, W. H., Teukolsky, S. A., Vetterling, W. T., & Flannery, B. P. 2007, *Numerical Recipes 3rd Edition: The Art of Scientific Computing*, 3rd edn. (New York: Cambridge University Press)
- Prša, A. & Zwitter, T. 2005, *ApJ*, 628, 426
- Rossiter, R. A. 1924, *ApJ*, 60, 15
- Rucinski, S. M. 1992, *AJ*, 103, 960
- Rucinski, S. M. 2007, *MNRAS*, 382, 393
- Stepień, K. 2006, *Acta Astron.*, 56, 347
- Stepień, K. & Gazeas, K. 2012, *Acta Astron.*, 62, 153
- Szymański, M., Kubiak, M., & Udalski, A. 2001, *Acta Astron.*, 51, 259
- Tamuz, O., Mazeh, T., & Zucker, S. 2005, *MNRAS*, 356, 1466
- Torres, G. 2013, *Astron. Nachr.*, 334, 4
- Torres, G., Andersen, J., & Giménez, A. 2010, *A&AR*, 18, 67
- Wilson, R. E. & Devinney, E. J. 1971, *ApJ*, 166, 605